Stability and electronic properties of GaN phases with inversion symmetry to inherently inhibit polarization

Anan Sun,[1] Shang-Peng Gao,[1,*] and Gong Gu[2,†]
[1]Department of Materials Science, Fudan University, Shanghai 200433, China
[2]Department of Electrical Engineering and Computer Science, University of Tennessee, Knoxville, Tennessee 37996, USA

(Received 22 July 2019; published 23 October 2019)

Two centrosymmetric gallium nitride phases, one with a body-centered-tetragonal structure (bct-GaN) and the other base-centered orthorhombic (*Z*-GaN), are predicted. The inversion symmetry inherently inhibits spontaneous polarization, and more importantly, piezoelectric polarization regardless of heteroepitaxial growth direction and even in the presence of shear strain, offering alternative solutions to the polarization-induced electrostatic field problem encountered by group-III nitride-based light-emitting diodes (LEDs), beyond those promised by nonpolar and semipolar wurtzite (w-GaN) and zinc-blende GaN. Density functional theory calculations, validated by agreement with experiment for w-GaN, reveal equilibrium structures, phonon dispersions, and band structures of bulk bct-GaN and *Z*-GaN. To ensure their stability at room temperature, we first carry out an analysis of dynamical and thermal stability using phonon calculations and molecular dynamics simulations, which indicate that these centrosymmetric structures are dynamically stable and remain stable at high temperature. Moreover, the relative stability of GaN polymorphs is highly dependent on sample thickness. We predict that bct-GaN and *Z*-GaN are energetically more favorable than w-GaN for freestanding ultrathin films up to 47 and 70 layers, respectively, thus suggesting the possibility of the kinetic growth of these two phases. The *GW* self-energy corrected, direct band gaps of bct-GaN and *Z*-GaN are close to the w-GaN value, promising LED applications in the same spectral ranges.

DOI: 10.1103/PhysRevMaterials.3.104604

I. INTRODUCTION

Gallium nitride, with a continuous alloy system spanning a large spectral range, forms the material foundation for commercial blue and green light-emitting diodes (LEDs), which are currently grown on *c*-plane sapphire substrates, where thermodynamically stable wurtzite GaN (w-GaN) naturally grows in the polar [0001] direction [1–3]. Low symmetry of the wurtzite structure gives rise to spontaneous polarization along this singular polar direction, and strains in pseudomorphic heterojunctions between lattice-mismatched alloys lead to piezoelectric polarization [4,5]. The total spontaneous and piezoelectric polarization discontinuities at the heterointerfaces induce polarization charges, which in turn result in strong electrostatic fields that tilt the energy bands [1]. The band tilting reduces the electron-hole overlap and thus limits the LED efficiency. Therefore, elimination or reduction of polarization-induced electrostatic fields along the growth direction, i.e., the LED heterojunction stacking direction, is highly desired and actively pursued.

Nonpolar w-GaN, grown in a direction perpendicular to [0001], is free of spontaneous or piezoelectric polarization in the growth direction [3] but suffers from undesirable surface morphology [1,2]. Semipolar w-GaN, grown in a direction at an angle from [0001], has thus recently become a more promising compromise [1]. To achieve the more desirable total elimination of spontaneous and piezoelectric polarization, zinc-blende GaN (zb-GaN), a metastable phase of higher symmetry, has been pursued for the intrinsic absence of spontaneous polarization and the lack of piezoelectric polarization when grown along [001], both due to symmetry [3]. If grown in other directions, e.g., [111], however, tensile strains in the plane of the heterointerface contain shear strain components in the cubic coordinate [5], giving rise to piezoelectric polarization that limits the substrate and orientation options. As attested by recent device demonstrations [1], the metastable phase zb-GaN can be kinetically grown to achieve device quality. Hence, a search for GaN polymorphs inherently free of both spontaneous and piezoelectric polarization may broaden potential solutions to the internal polarization field problem.

The phase space of GaN has not been extensively explored. Besides the well-known wurtzite and zinc-blende phases, only two other polymorphs have been reported. A polymorph observed under high hydrostatic pressure was identified by density functional theory (DFT) calculation [6] and subsequently verified by experiment [7] to be rocksalt GaN. Under uniaxial compression [8] or for films consisting of less than a certain number of layers [9], GaN with a hexagonal layered structure (denoted as h-GaN) was predicted to be energetically more favorable than w-GaN, also based on DFT. Our phonon calculations and molecular dynamics simulations (Fig. 1) indicate that the bulk structure of h-GaN is dynamically unstable, implying that h-GaN can only be stabilized in the ultrathin limit

*gaosp@fudan.edu.cn
†ggu1@utk.edu

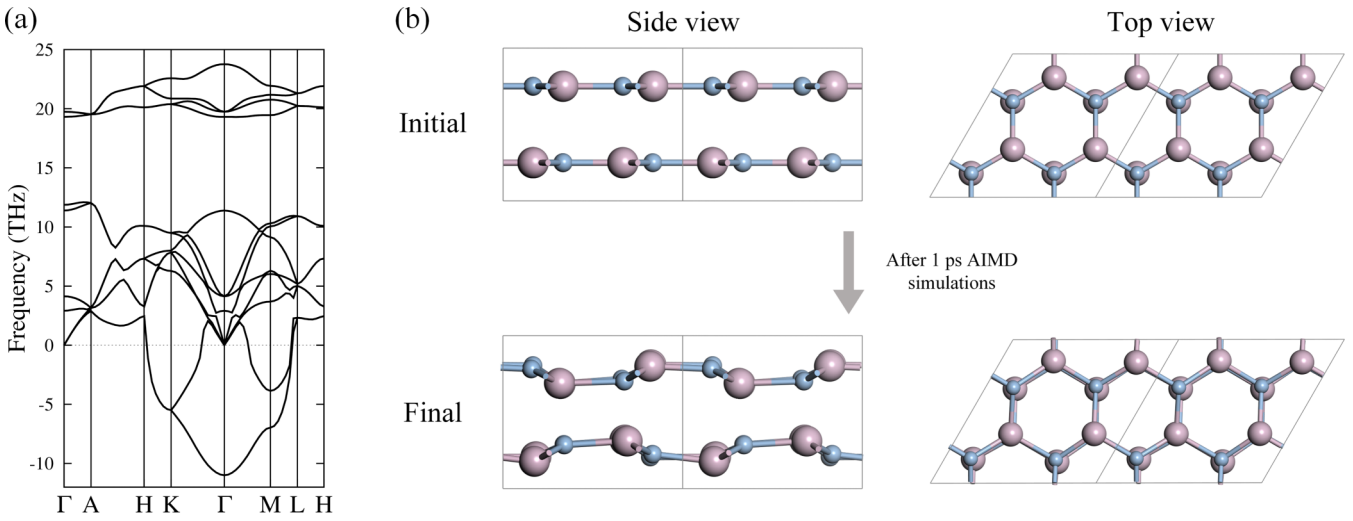

FIG. 1. (a) Phonon dispersion curves of bulk h-GaN. Imaginary frequencies that appear near the Γ point indicate dynamical instability. (b) Snapshots of the initial and final atom configurations of h-GaN in 1-ps AIMD simulations performed at 273 K. The flat hexagonal layers of h-GaN become buckled after AIMD simulations. This buckled structure will optimize to a body-centered tetragonal structure in structural relaxation. Larger pink and smaller blue spheres represent Ga and N atoms, respectively. These calculations are performed using the CASTEP code.

or under specific stress. Here, we report the computational discovery of two centrosymmetric GaN polymorphs metastable under ambient conditions. The two phases (Fig. 2), inherently free of both spontaneous and piezoelectric polarization due to symmetry, have the body-centered-tetragonal (bct-GaN) and the base-centered-orthorhombic (*Z*-GaN) structures, similar to the bct (bct-BN [10], bct-ZnO [11,12], bct-C [13]), and *Z* (*Z*-BN [14], *Z*-carbon [15,16]) polymorphs of other octet compounds or carbon, respectively. Phonon dispersions and band structures of bct-GaN and *Z*-GaN, as well as w-GaN for comparison, are investigated by DFT, revealing dynamic stability and direct band gaps for bct-GaN and *Z*-GaN, both of which are desired properties for LED materials. The thermal stability of bct-GaN and *Z*-GaN at elevated temperatures is tested using *ab initio* molecular dynamics simulations (AIMD). In addition to the bulk calculations, considering that the relative stability of GaN polymorphs in the case of two-dimensional ultrathin films is expected to be different from the bulk case, as suggested by the study mentioned above on h-GaN, we investigate the relative stability of ultrathin films of w-GaN, h-GaN, bct-GaN, and *Z*-GaN.

II. COMPUTATIONAL METHODS

A. DFT calculation details

For structural optimizations and phonon calculations, the ABINIT 8.2.2 code [17,18] is used with a cutoff energy of 1089 eV (40 hartrees) for the plane-wave basis set. We employ the optimized norm-conserving Vanderbilt pseudopotentials [19] and the generalized gradient approximation (GGA) proposed by Perdew, Burke, and Ernzerhof (PBE) [20] with the DFT-D3 dispersion correction [21] based on Becke-Jonson (BJ) damping [22] to describe long-range correlations. Structural optimizations are conducted using the Broyden-Fletcher-Goldfarb-Shanno (BFGS) minimization [23], with Monkhorst-Pack [24] *k*-point grids that are 12 × 12 × 10 for w-GaN, 6 × 6 × 10 for bct-GaN, and 8 × 4 × 14 for *Z*-GaN, yielding zero-pressure structural properties. The calculations of phonon dispersions and band structures are based on the equilibrium structures obtained from structural optimizations. Phonon calculations are based on the density-functional perturbation theory (DFPT) [25], using **q** point grids of 8 × 8 × 6 for w-GaN, 6 × 6 × 8 for bct-GaN, and 6 × 3 × 10 for *Z*-GaN.

We perform AIMD simulations using the CASTEP code [26] to evaluate the thermal stability of bct-GaN and *Z*-GaN at high temperature. In AIMD simulations, a 32-atom supercell (2 × 1 × 2 for bct-GaN and 1 × 1 × 2 for *Z*-GaN) is used. The AIMD simulations are performed in *NpT* ensemble at 600 K and 0 Pa for 10 ps with a time step of 2 fs, using the Nosé-Hoover chain thermostat [27] and the Andersen-Hoover barostat [28–31] to control temperature (T) and pressure (p), respectively.

The calculations of ultrathin films also use the CASTEP code. Supercell slabs are separated by a 10-Å-thick vacuum region to eliminate interactions between adjacent slabs. We use "on-the-fly" generated ultrasoft pseudopotentials and PBE-GGA [20] with DFT-D2 dispersion correction [32]. A cutoff energy of 570 eV and *k*-point grids of 9 × 9 × 1 for w-GaN and h-GaN, 8 × 5 × 1 for bct-GaN, and 8 × 2 × 1 for *Z*-GaN slabs are adopted.

B. Band-gap determination using *GW* method

To overcome the well-known underestimation of semiconductor band gaps by the standard Kohn-Sham procedure, we use the *GW* method as implemented in the ABINIT 8.2.2 code, which incorporates self-energy corrections, to obtain accurate quasiparticle energies and band gaps. The *GW* calculations follow the standard one-shot G_0W_0 approach [33–35] from a starting point of DFT calculations based on local density approximation (LDA) and Fritz-Haber-Institute (FHI)

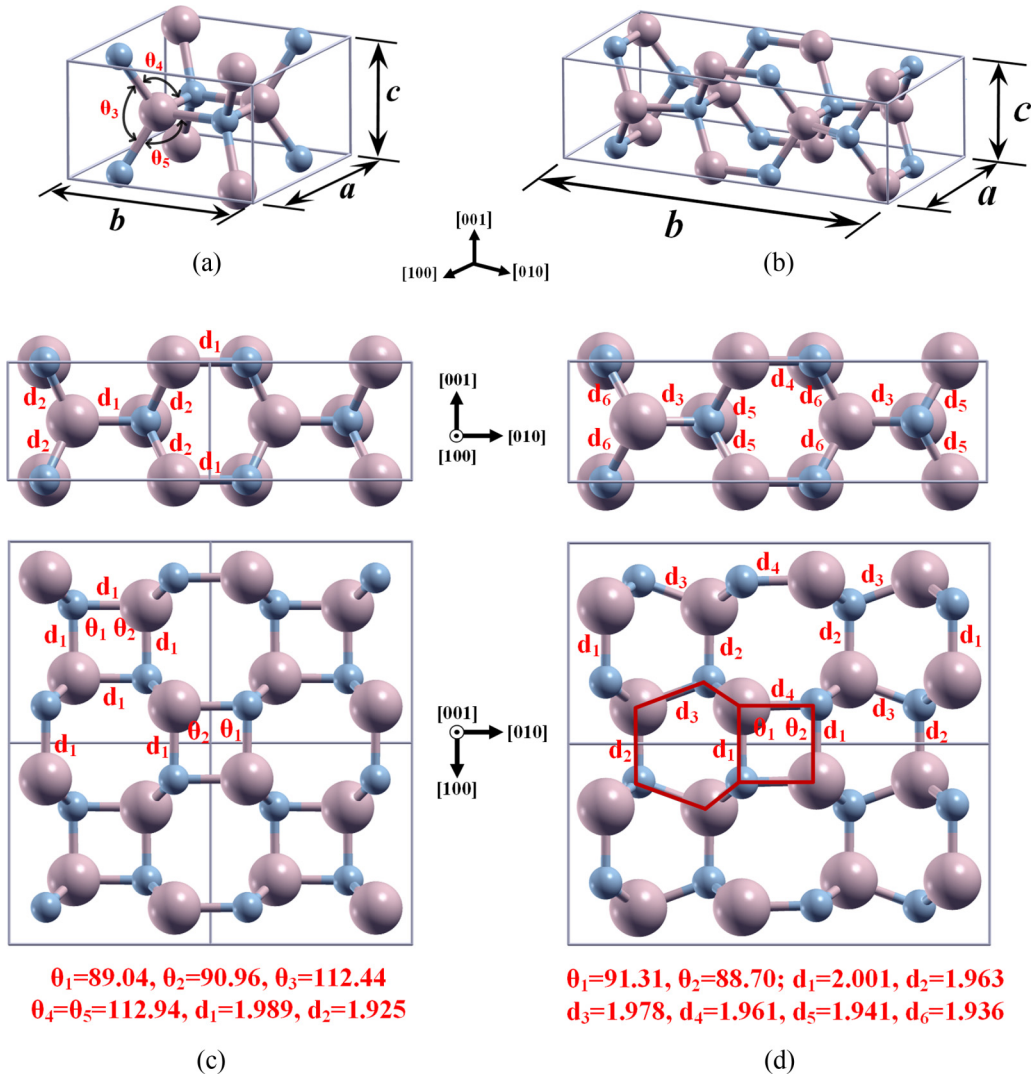

FIG. 2. Unit cells for (a) bct-GaN and (b) Z-GaN, and views along [100] and [001] directions for (c) bct-GaN and (d) Z-GaN. Lattice parameters a, b, c are indicated. Bond angles are denoted by $\theta_i (i = 1-5)$, and bond lengths, $d_i (i = 1-6)$. Larger pink and smaller blue spheres represent Ga and N atoms, respectively.

pseudopotentials (the Troullier-Martins scheme) [36]. The k-point grids of $12 \times 12 \times 8$, $4 \times 4 \times 6$, and $4 \times 2 \times 6$ are used for w-GaN, bct-GaN, and Z-GaN, respectively. The plasmon-pole approximation [35] is used for the evaluation of the screened Coulomb interaction. The cutoff energy for the dielectric matrix is set to 435 eV (16 hartrees). The numbers of bands used in the calculations of the screening and the self-energy are set to 200, 400, and 800 for w-GaN, bct-GaN, and Z-GaN, respectively.

III. RESULTS AND DISCUSSION

A. Crystal structures of bct-GaN and Z-GaN

Although long-range dispersion corrections to DFT-GGA are less crucial in a dense system like w-GaN than in sparse systems such as layered materials and molecular crystals, the agreement between calculated and experimental lattice parameters can be improved by the inclusion of dispersion corrections. As such, our GGA results with dispersion corrections ($a = 3.196$ Å, $c = 5.208$ Å) are closer to the experimental values ($a = 3.190$ Å, $c = 5.189$ Å) [37] than our GGA results without dispersion corrections ($a = 3.218$ Å and $c = 5.242$ Å). Lattice parameters of the three GaN polymorphs calculated by DFT-GGA with dispersion corrections are listed in Table I, along with experimental values and reported GGA and LDA results of w-GaN for comparison. Our results, closely matching experimental values, lie between previous results of GGA [38] and LDA [39], showing that the combination of GGA and dispersion corrections reduces the excessive correction to the LDA overbinding [40]. Excellent agreement with experimental lattice parameters for w-GaN indicates the accurate determination of structures for the two new phases, laying down the groundwork for the phonon dispersion and energy-band-structure calculations.

The structure of bct-GaN (Fig. 2) is described as a simple tetragonal Bravais lattice with a basis consisting of two oppositely oriented, planar, four-atom rings parallel to (001), each made of alternating Ga and N atoms, displaced along [111] by

TABLE I. Space groups, equilibrium lattice parameters and Wyckoff positions of atoms for w-GaN, bct-GaN, and Z-GaN at zero pressure. Experimental and previous theoretical results for w-GaN are included for comparison.

Phases	Space groups	Equilibrium lattice parameters (Å)	Wyckoff positions of atoms
w-GaN	$P6_3mc$	$a = b = 3.196$, 3.190,[a] 3.245,[b] 3.162[c] $c = 5.208$, 5.189,[a] 5.296,[b] 5.142[c]	Ga $2b$ (1/3, 2/3, 0) N $2b$ (1/3, 2/3, 0.377)
bct-GaN	$P4_2/mnm$	$a = b = 5.491$, $c = 3.200$	Ga $4f$ (0.180, 0.180, 0) N $4g$ (0.817, 0.183, 0)
Z-GaN	$Pbam$	$a = 5.289$, $b = 11.097$, $c = 3.205$	Ga $4g$ (0.185, 0.588, 0), $4h$ (0.819, 0.166, 0.5) N $4g$ (0.694, 0.088, 0), $4h$ (0.190, 0.167, 0.5)

[a]Reference [37], experiment.
[b]Reference [38], DFT-GGA.
[c]Reference [39], DFT-LDA.

half the unit cell diagonal from each other. There are two types of Ga-N bonds in bct-GaN with lengths 1.989 and 1.925 Å, denoted by d_1 and d_2 in Fig. 2(c), respectively. Z-GaN shares structural similarity with bct-GaN and can be viewed as a simple orthorhombic Bravais lattice with a 16-atom basis consisting of two oppositely oriented eight-atom clusters [one delineated by the red outline in Fig. 2(d)], displaced along [110] by half the base diagonal from each other. There are six different types of Ga-N bonds in Z-GaN with lengths 2.001, 1.963, 1.978, 1.961, 1.941, and 1.936 Å, denoted by d_i ($i = 1 - 6$), respectively.

All atoms are fourfold coordinated in bct-GaN and Z-GaN, as in w-GaN and zb-GaN. Familiar honeycomblike patterns are seen when both bct-GaN [Fig. 2(c)] and Z-GaN [Fig. 2(d)] are viewed along [100], as w-GaN along [0001]. The unit cells of both bct-GaN and Z-GaN contain parallelograms composed of four atoms (two Ga and two N), in which the bond angles Ga-N-Ga and N-Ga-N (denoted by θ_1 and θ_2, respectively) are $\theta_1 = 89.04^\circ$, $\theta_2 = 90.96^\circ$ for bct-GaN and $\theta_1 = 91.31^\circ$, $\theta_2 = 88.70^\circ$ for Z-GaN. Figure 2(a) shows that the bond angles in the Ga-centered tetrahedron in bct-GaN are $\theta_2 = 90.96^\circ$, $\theta_3 = 112.44^\circ$, $\theta_4 = \theta_5 = 112.94^\circ$, indicating distorted tetrahedral coordination with regard to w-GaN and zb-GaN due to the formation of parallelograms. Similarly, Z-GaN also exhibits distorted tetrahedral coordination to accommodate the near-square parallelograms. While each of the two new phases exhibits unequal bond lengths due to the coordination distortion, the average bond lengths, 1.957 Å for bct-GaN and 1.963 Å for Z-GaN, are close to bond lengths of w-GaN (1.961 Å along [0001], 1.954 Å for other bonds) and zb-GaN (1.949 Å) [41]. The most important feature of the two structures (bct-GaN and Z-GaN belonging to space

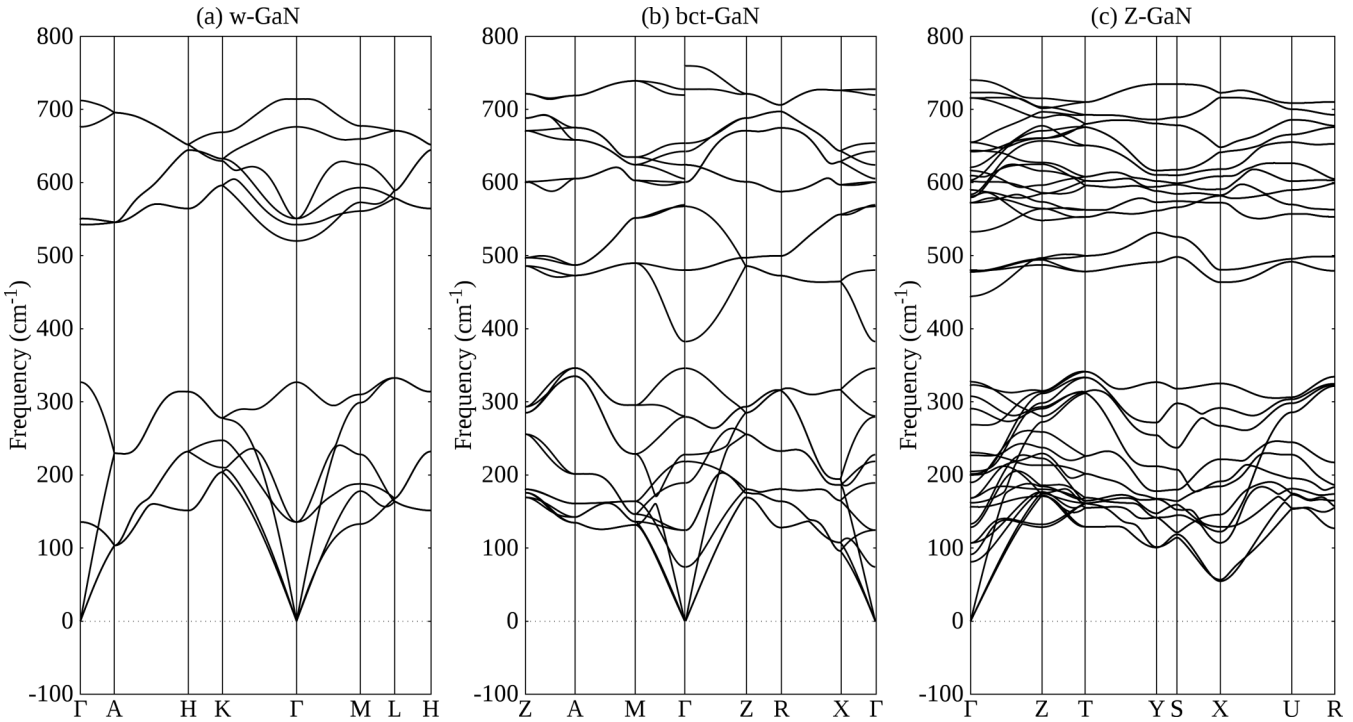

FIG. 3. Calculated phonon dispersion curves for (a) w-GaN, (b) bct-GaN, and (c) Z-GaN. A horizontal line is plotted at zero frequency for easy visualization, and negative values signify imaginary frequencies, which are absent throughout the entire Brillouin zone for each of the polymorphs.

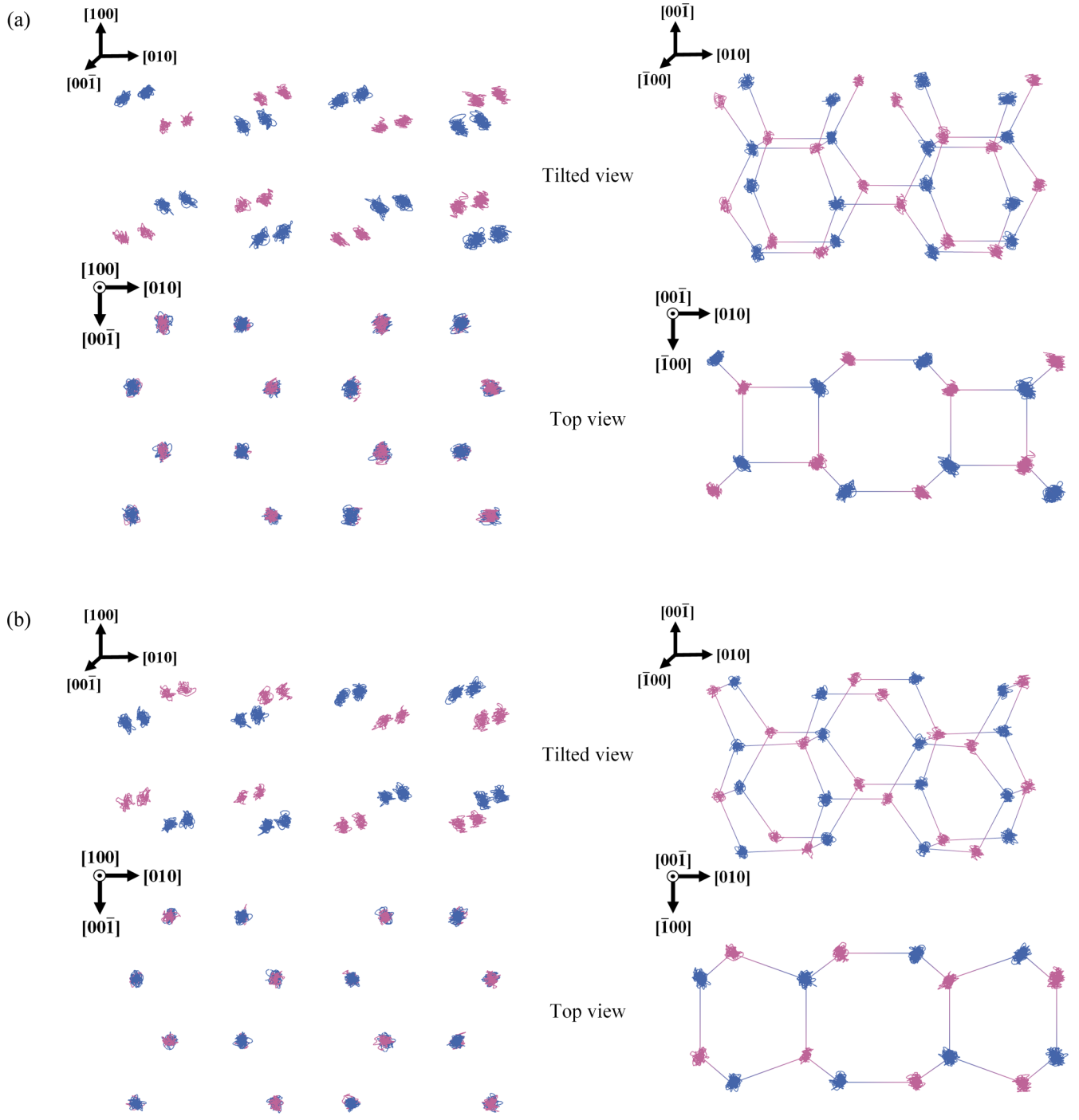

FIG. 4. Trajectories of atoms in the supercells of (a) bct-GaN and (b) Z-GaN during the last 2 ps of 10-ps AIMD simulations performed at 600 K. The trajectories viewed along different directions are presented. On the right panel, the chemical bonds are drawn to guide the eye. The trajectories of Ga and N atoms are depicted in pink and blue, respectively.

groups $P4_2/mnm$ and *Pbam*, respectively) is inversion symmetry, rendering them free of not only spontaneous but also piezoelectric polarization, regardless of orientation and even in the presence of shear strain.

B. Stability: Phonon calculations and AIMD simulations

The desired inversion symmetry comes at an energy cost associated with the coordination distortion, warranting a quantitative thermodynamic stability analysis. Here, the total internal energy is taken as an indicator of thermodynamic stability. Indeed, the total energies referenced to the thermodynamically stable phase w-GaN are 120 and 78.1 meV/GaN unit for bct-GaN and *Z*-GaN, respectively, well above 14.4 meV/GaN unit for zb-GaN. Nevertheless, a metastable phase can exist despite high internal energy as long as it is a local minimum of the energy surface and hence is dynamically stable. We therefore calculate phonon

dispersions of the two polymorphs as the first test of dynamical stability.

Phonon dispersions are calculated for bct-GaN and *Z*-GaN, along with w-GaN, again to provide validation and comparison. Phonon dispersion curves in Fig. 3 show 12, 24, and 48 phonon branches for w-GaN, bct-GaN, and *Z*-GaN, respectively, stemming from their four-, eight-, and 16-atom unit cells. The phonon frequencies and the overall features of the dispersion curves for w-GaN are in agreement with previous calculations and experiments [42–44]. For example, there are only eight modes along the $\Gamma \rightarrow A$ direction and four modes at the *A* point due to degeneracy, as shown in Fig. 3(a). The excellent agreement validates our calculation scheme, lending confidence to the results for bct-GaN and *Z*-GaN. We have noticed the apparent discontinuities in dispersion curves at the Γ point, displayed in Fig. 3(b) for bct-GaN (the Γ-point phonon frequencies along the $M \rightarrow \Gamma$ direction and the $Z \rightarrow \Gamma$ direction are not identical), and attributed them to the dependence of the calculated LO-TO splitting on the direction in which the nonanalytical correction to the Γ point phonon frequencies is calculated in the limit $\mathbf{q} \rightarrow 0$ [25]. Most importantly, imaginary phonon frequencies are absent throughout the entire Brillouin zone for both bct-GaN and *Z*-GaN, confirming their dynamic stability. We note that dynamic stability as manifested by the absence of imaginary phonon frequencies is only a necessary condition for the existence and synthesis of theoretically predicted polymorphs; further work is needed to investigate the feasibility of synthesis of bct-GaN and *Z*-GaN.

Having confirmed the dynamic stability of bct-GaN and *Z*-GaN against small displacements, we further performed AIMD simulations (600 K, 0 Pa, 10 ps) to evaluate their thermal stability at high temperature. In Fig. 4, we present the trajectories of atoms, viewed along different directions in 32-atom supercells of bct-GaN and *Z*-GaN during the last 2 ps of 10-ps AIMD simulations. At temperature as high as 600 K, despite small displacements of atoms, the atoms are well localized around the equilibrium positions and the overall atomic configurations of bct-GaN and *Z*-GaN are maintained, confirming the thermal stability of the found phases at high temperature.

C. Band structures

To determine the band structures of bct-GaN and *Z*-GaN, which are of critical importance for their potential use in LEDs, the *GW* method is utilized to calculate quasiparticle energies at high-symmetry *k* points. Once again, w-GaN provides comparisons with the experimental band gap and previous calculations. With no experimental structural parameters for the predicted bct-GaN and *Z*-GaN, our calculated values (Table I) are used, as their accuracy has been justified by the excellent agreement with experiment for w-GaN. The band structures of three GaN polymorphs are displayed in Fig. 5. Our DFT-LDA calculations show that w-GaN, bct-GaN, and *Z*-GaN have direct band gaps of 2.11, 2.08, and 2.04 eV at the Γ point, respectively, exhibiting remarkable similarities to each other in electronic properties, perhaps due to the structural similarities. Figure 5(a) shows that the overall shapes of the bands of w-GaN agree well with previous theoretical calculations [45–47] and experimental measurements [48]. While our LDA band gap of w-GaN (2.11 eV) corresponds

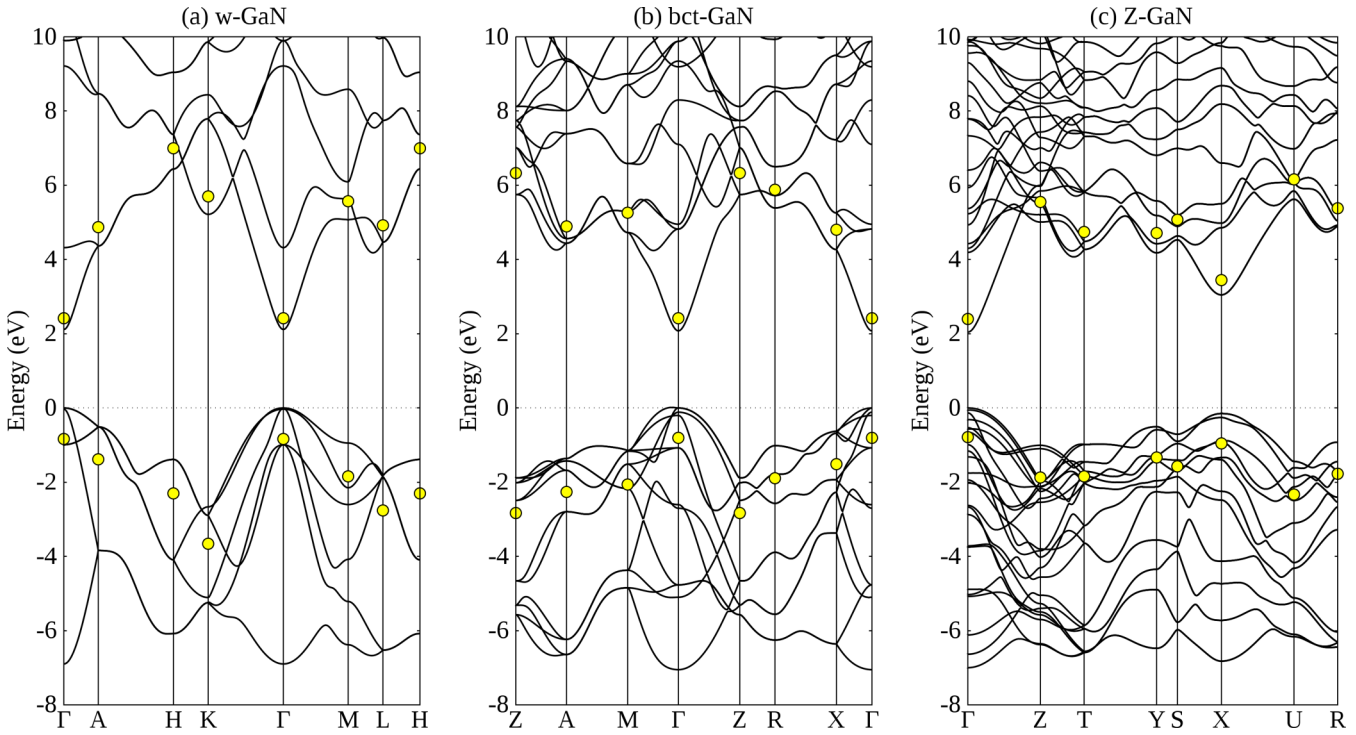

FIG. 5. Calculated band structures of (a) w-GaN, (b) bct-GaN, and (c) *Z*-GaN. Black curves are energy dispersion curves calculated by LDA, while yellow circles indicate *GW*-corrected energies at high-symmetry *k* points for the highest valence and lowest conduction bands. The LDA valence-band maximum is set to 0 eV and indicated by a horizontal dotted line for easy visualization.

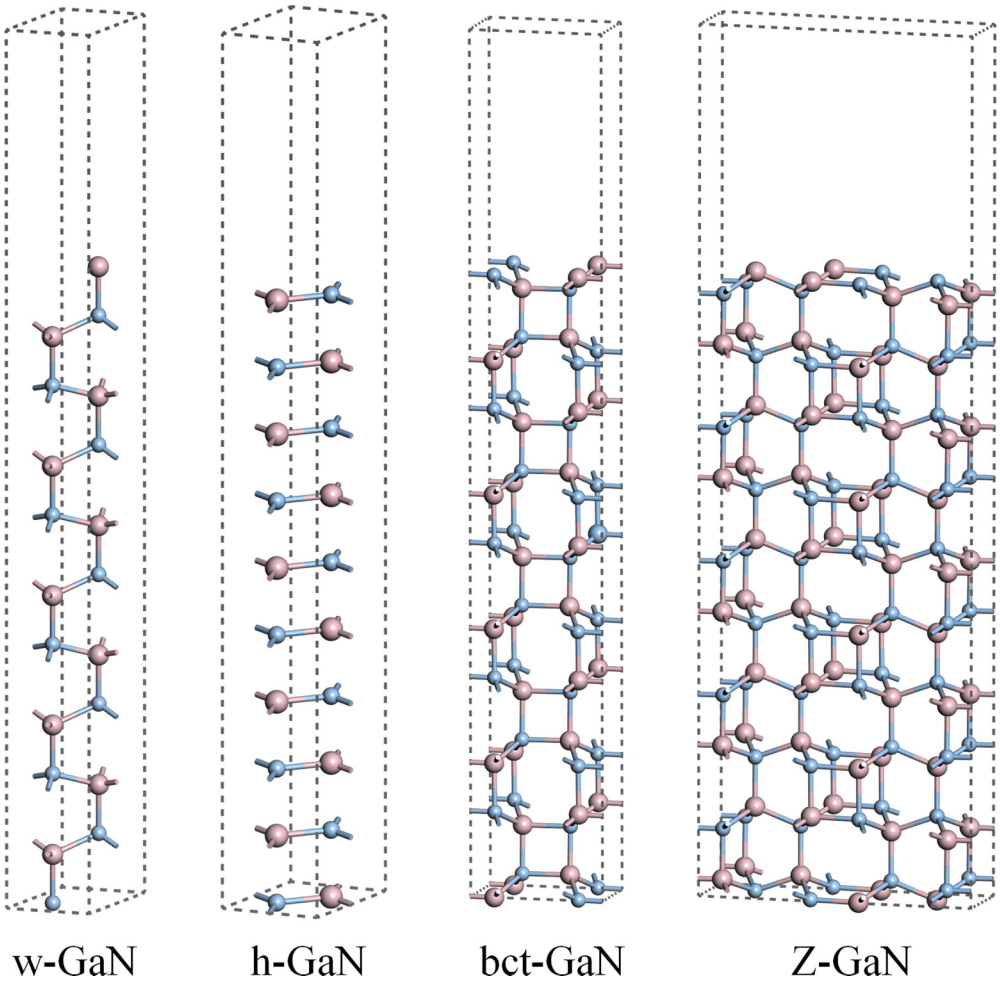

FIG. 6. Supercells of ten-layer slabs of w-GaN, h-GaN, bct-GaN, and *Z*-GaN with {0001}, (0001), (100), and (100) surfaces, respectively. Larger pink spheres represent Ga cations and smaller blue ones represent N anions.

well with the published DFT-LDA value (2.13 eV) [38], it is nevertheless considerably smaller than the experimental value (3.39 eV) [49]. The *GW* calculations yield larger energy gaps at high-symmetry points for w-GaN, in better agreement with experimental results [48]. The *GW* band gaps of w-GaN, bct-GaN, and *Z*-GaN are 3.26, 3.22, and 3.18 eV, respectively, which remain direct at the Γ point and close not only to each other, but also to the experimental band gap of w-GaN, although the *GW* band gap of w-GaN is still 0.13 eV smaller than the experimental value, suggesting that the calculated band gaps for bct-GaN and *Z*-GaN are slightly underestimated by similar amounts. It follows that our predicted direct wide band-gap bct-GaN and *Z*-GaN, if successfully synthesized, are promising materials for use in GaN-based LEDs.

D. Relative stability of GaN polymorphs in the case of ultrathin films

Figure 6 shows the supercells of ten-layer slabs of w-GaN, h-GaN, bct-GaN, and *Z*-GaN used for ultrathin-film calculations. The number of layers is counted such that two adjacent monolayers in w-GaN, bct-GaN, and *Z*-GaN slabs are considered as one layer. The variation of the energies per GaN unit of the slabs of four GaN polymorphs with the number of layers (2–20) is shown in Fig. 7(a). The slabs of all four polymorphs demonstrate the same trends that the energies per GaN unit decrease with the number of layers, converging to the bulk energies and indicating the decreasing contribution of surface energies. For very thin films (less than four layers), h-GaN has the lowest energy, w-GaN the highest, while bct-GaN and *Z*-GaN are in between. As the film thickness increases, the energies of bct-GaN and *Z*-GaN become lower than that of h-GaN at four layers and six layers, respectively. For thicker films with 14 or more layers, the energy of w-GaN falls below that of h-GaN. Note that the bct-GaN and *Z*-GaN slabs are the most energetically favorable and close in energy due to their structural similarity for films between six and 20 layers. At 16 layers, the bct-GaN slabs become less stable than *Z*-GaN, corresponding to our bulk calculations [see the inset in Fig. 7(a)].

To estimate the relative stability of thicker films of these polymorphs, the calculated energies of the w-GaN, bct-GaN, and *Z*-GaN slabs (E_{slab}) for the number of layers $n_{\text{layers}} \geqq 10$ are fitted to the linear functions of the form $E_{\text{slab}} = 2AE_{\text{surf}} + 0.5n_{\text{layers}}E_{\text{bulk}}$, where $2A$ is the area of two surfaces per supercell of the slab, E_{bulk} is the bulk energy per unit cell of four polymorphs, and the surface energy E_{surf} is assumed to be constant, as described by Morgan [50]. The resulting

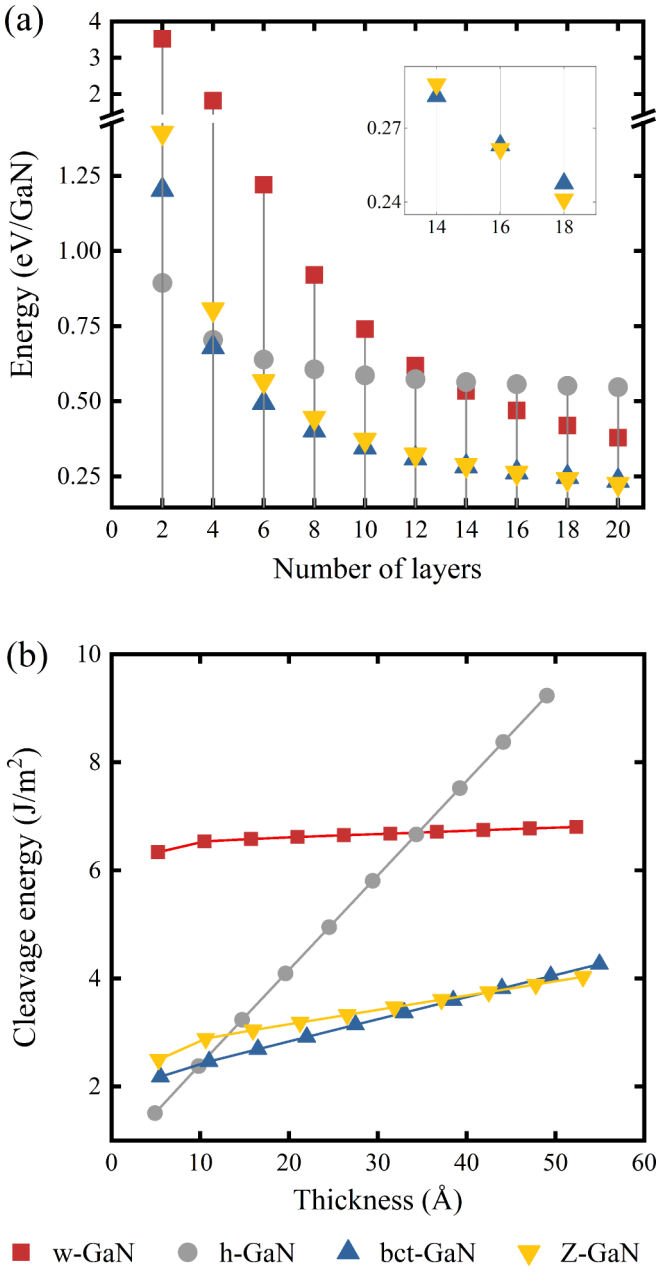

FIG. 7. (a) Calculated energies per GaN unit as a function of the number of layers for w-GaN, h-GaN, bct-GaN, and *Z*-GaN slabs. The energies are plotted with respect to that of bulk w-GaN, which is taken as a reference. The inset shows an enlarged view of the range 14–18 layers. (b) Calculated cleavage energies as a function of the slab thickness for w-GaN, h-GaN, bct-GaN, and *Z*-GaN slabs.

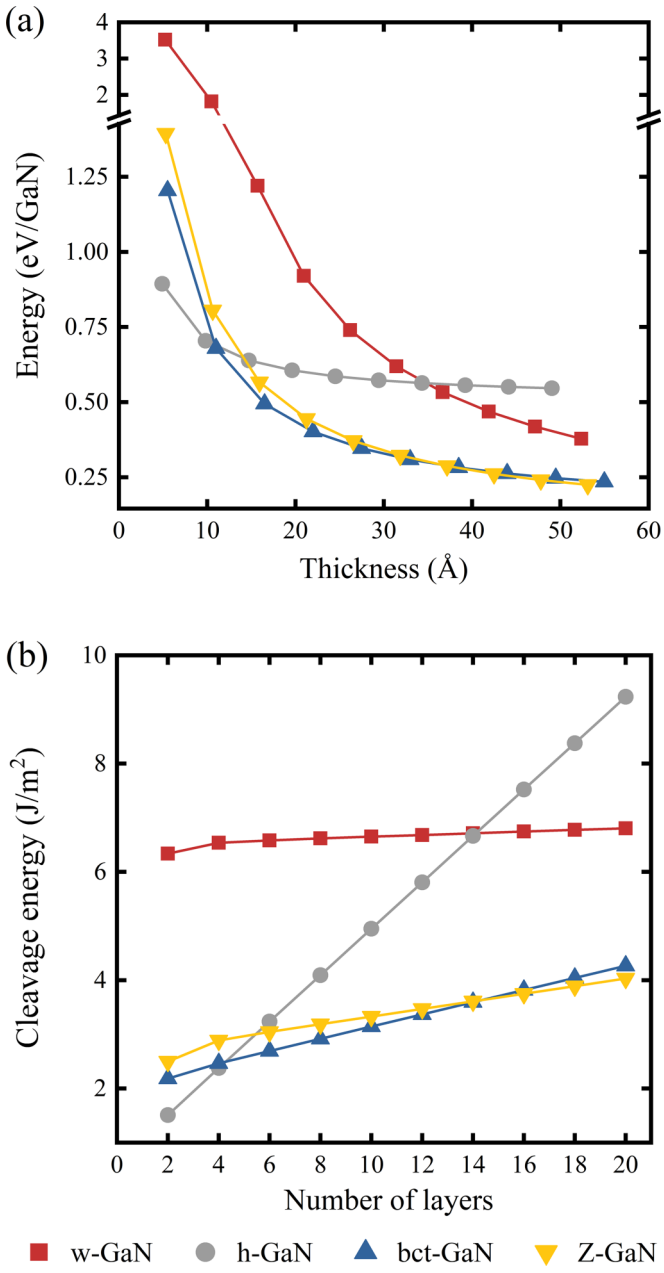

FIG. 8. (a) Calculated energies per GaN unit as a function of the slab thickness for w-GaN, h-GaN, bct-GaN, and *Z*-GaN slabs. The energies are plotted with respect to that of bulk w-GaN, which is taken as a reference. (b) Calculated cleavage energies as a function of the number of layers for w-GaN, h-GaN, bct-GaN, and *Z*-GaN slabs.

curves of the energies per GaN unit of the w-GaN and bct-GaN (*Z*-GaN) slabs cross at $n_{\text{layers}} \approx 47(70)$, at which w-GaN will become energetically more favorable than bct-GaN (*Z*-GaN), corresponding to the bulk case.

The cleavage energies of w-GaN, h-GaN, bct-GaN, and *Z*-GaN slabs are shown in Fig. 7(b), plotted as a function of slab thickness. The slab thickness is defined as the number of unit cells per supercell of the slab times the corresponding lattice parameter. The cleavage energies are calculated by subtracting the energy of bulk w-GaN from the energies of slabs and dividing by the area of both surfaces per supercell of slabs, following the scheme adopted by Freeman *et al.* [9] The relative stability of four polymorphs indicated by the comparison of the cleavage energies [Fig. 7(b)] is consistent with that indicated by the comparison of the energies [Fig. 7(a)]. The cleavage energy of the w-GaN slabs converges to 6.8 J/m^2 with increasing film thickness, while the cleavage energies of the h-GaN, bct-GaN, and *Z*-GaN slabs increase nearly linearly with film thickness. For very thin films, h-GaN has the lowest cleavage energy. As the films increase in thickness, h-GaN becomes less stable with respect to bct-GaN (at ∼1.0 nm), *Z*-GaN (at ∼1.3 nm), and w-GaN (at ∼3.4 nm). For films more

than ∼4.2 nm thick, the cleavage energy of *Z*-GaN falls below that of bct-GaN. The relatively high energy and high cleavage energy for the very thin films of w-GaN can be attributed to its polar unit cell which has higher surface energy than those of nonpolar h-GaN, bct-GaN, and *Z*-GaN, as pointed out before in the ZnO case by Morgan [50].

Additionally, the variation of energies with slab thickness of four polymorphs is shown in Fig. 8(a). For very thin films, h-GaN has the lowest energy, w-GaN the highest, while bct-GaN and *Z*-GaN are in between. As the film thickness increases, the energies of bct-GaN and *Z*-GaN become lower than that of h-GaN at 1.1 nm and 1.4 nm, respectively. For thicker films (more than 3.5 nm thick), the energy of w-GaN falls below that of h-GaN. At 3.7 nm, the bct-GaN slabs become less stable than Z-GaN. Figure 8(b) displays the variation of cleavage energies with the number of layers for the slabs of four polymorphs. For very thin films, h-GaN has the lowest cleavage energy. As the films increase in thickness, h-GaN becomes less stable with respect to bct-GaN (at four layers), *Z*-GaN (at six layers), and w-GaN (at 14 layers). For films consisting of more than 15 layers, the cleavage energy of *Z*-GaN falls below that of bct-GaN. Note that the estimated critical thickness holds good only in the freestanding case; the favorable phase can be biased by the selected substrate in experimental growth.

IV. CONCLUSIONS

Two GaN polymorphs, bct-GaN and *Z*-GaN, have been predicted. We have performed DFT calculations to investigate equilibrium structures, phonon dispersions, and band structures of bct-GaN and *Z*-GaN, as well as w-GaN, the results of which closely match previous theoretical and experimental results and thus validate our calculation scheme. The phonon dispersions indicate that bct-GaN and *Z*-GaN are dynamically stable. The AIMD simulations at 600 K further prove that bct-GaN and *Z*-GaN remain stable at high temperature. The *GW* calculations of band structures show that bct-GaN and *Z*-GaN have direct band gaps at the Γ point with values similar to that of w-GaN, therefore suitable for LED applications in the same spectral ranges if successfully grown. To investigate phase competition of GaN growth in the ultrathin film stage, we have extended our study to the relative stability of films of four GaN polymorphs, w-GaN, h-GaN, bct-GaN, and *Z*-GaN with varying numbers of layers. For very thin films (<four layers), h-GaN which is dynamically unstable in bulk form, is the most stable of four polymorphs. As the film thickness increases, bct-GaN (*Z*-GaN) becomes energetically more favorable than both h-GaN and w-GaN and persists up to 47 (70) layers, suggesting the possibility of their growth under appropriate experimental conditions. And once the growth of bct-GaN and *Z*-GaN is initiated in favorable thin-film condition, they can continue to grow to bulk size due to their dynamical and thermal stability.

Note that bct-GaN and *Z*-GaN are both centrosymmetric and hence possess neither spontaneous polarization nor piezoelectric polarization regardless of heterojunction stacking orientation and even in the presence of shear stress, broadening potential solutions to the internal polarization field problem beyond those offered by zb-GaN and nonpolar and semipolar w-GaN. This unique advantage merits further investigations, and the metastability and the feasibility of kinetic growth of these predicted GaN polymorphs and the associated alloys with the same crystal structures remain to be confirmed by experiment. We anticipate this work to offer an alternative approach to the further enhancement of the luminous efficiency of GaN-based LEDs.

ACKNOWLEDGMENTS

This work was supported by the Natural Science Foundation of Shanghai (Grant No. 19ZR1404300), by the Innovation Program of Shanghai Municipal Education Commission (Grant No. 15ZZ001), and by U.S. Army Research Office (Grant No. W911NF1810382).

[1] Y. J. Zhao, H. Q. Fu, G. T. Wang, and S. Nakamura, Toward ultimate efficiency: Progress and prospects on planar and 3D nanostructured nonpolar and semipolar InGaN light-emitting diodes, Adv. Opt. Photon. **10**, 246 (2018).

[2] G. Q. Li, W. L. Wang, W. J. Yang, Y. H. Lin, H. Y. Wang, Z. T. Lin, and S. Z. Zhou, GaN-based light-emitting diodes on various substrates: A critical review, Rep. Prog. Phys. **79**, 056501 (2016).

[3] P. Waltereit, O. Brandt, A. Trampert, H. T. Grahn, J. Menniger, M. Ramsteiner, M. Reiche, and K. H. Ploog, Nitride semiconductors free of electrostatic fields for efficient white light-emitting diodes, Nature (London) **406**, 865 (2000).

[4] F. Bernardini and V. Fiorentini, Spontaneous versus piezoelectric polarization in III-V nitrides: Conceptual aspects and practical consequences, Phys. Status Solidi B **216**, 391 (1999).

[5] F. Bernardini, V. Fiorentini, and D. Vanderbilt, Spontaneous polarization and piezoelectric constants of III-V nitrides, Phys. Rev. B **56**, R10024 (1997).

[6] A. Munoz and K. Kunc, High-pressure phase of gallium nitride, Phys. Rev. B **44**, 10372 (1991).

[7] H. Xia, Q. Xia, and A. L. Ruoff, High-pressure structure of gallium nitride: Wurtzite-to-rocksalt phase transition, Phys. Rev. B **47**, 12925 (1993).

[8] K. Sarasamak, A. J. Kulkarni, M. Zhou, and S. Limpijumnong, Stability of wurtzite, unbuckled wurtzite, and rocksalt phases of SiC, GaN, InN, ZnO, and CdSe under loading of different triaxialities, Phys. Rev. B **77**, 024104 (2008).

[9] C. L. Freeman, F. Claeyssens, N. L. Allan, and J. H. Harding, Graphitic Nanofilms as Precursors to Wurtzite Films: Theory, Phys. Rev. Lett. **96**, 066102 (2006).

[10] B. Wen, J. J. Zhao, R. Melnik, and Y. J. Tian, Body-centered tetragonal BN: A novel sp^3 bonding boron nitride polymorph, Phys. Chem. Chem. Phys. **13**, 14565 (2011).

[11] J. Wang, A. J. Kulkarni, K. Sarasamak, S. Limpijumnong, F. J. Ke, and M. Zhou, Molecular dynamics and density functional studies of a body-centered-tetragonal polymorph of ZnO, Phys. Rev. B **76**, 172103 (2007).

[12] M.-R. He, R. Yu, and J. Zhu, Reversible wurtzite-tetragonal reconstruction in ZnO $(10\bar{1}0)$ surfaces, Angew. Chem. Int. Ed. **51**, 7744 (2012).
[13] P. A. Schultz, K. Leung, and E. B. Stechel, Small rings and amorphous tetrahedral carbon, Phys. Rev. B **59**, 733 (1999).
[14] C. Y. He, L. Z. Sun, C. X. Zhang, X. Y. Peng, K. W. Zhang, and J. X. Zhong, A novel superhard boron nitride phase, Phys. Chem. Chem. Phys. **14**, 10967 (2012).
[15] M. Amsler, J. A. Flores-Livas, L. Lehtovaara, F. Balima, S. A. Ghasemi, D. Machon, S. Pailhès, A. Willand, D. Caliste, S. Botti *et al.*, Crystal Structure of Cold Compressed Graphite, Phys. Rev. Lett. **108**, 065501 (2012).
[16] Z. S. Zhao, B. Xu, X.-F. Zhou, L.-M. Wang, B. Wen, J. L. He, Z. Y. Liu, H.-T. Wang, and Y. J. Tian, Novel Superhard Carbon: C-Centered Orthorhombic C_8, Phys. Rev. Lett. **107**, 215502 (2011).
[17] X. Gonze, B. Amadon, P. M. Anglade, J. M. Beuken, F. Bottin, P. Boulanger, F. Bruneval, D. Caliste, R. Caracas, M. Côté *et al.*, ABINIT: First-principles approach to material and nanosystem properties, Comput. Phys. Commun. **180**, 2582 (2009).
[18] X. Gonze, F. Jollet, F. A. Araujo, D. Adams, B. Amadon, T. Applencourt, C. Audouze, J. M. Beuken, J. Bieder, A. Bokhanchuk *et al.*, Recent developments in the ABINIT software package, Comput. Phys. Commun. **205**, 106 (2016).
[19] D. R. Hamann, Optimized norm-conserving Vanderbilt pseudopotentials, Phys. Rev. B **88**, 085117 (2013).
[20] J. P. Perdew, K. Burke, and M. Ernzerhof, Generalized Gradient Approximation Made Simple, Phys. Rev. Lett. **77**, 3865 (1996).
[21] S. Grimme, S. Ehrlich, and L. Goerigk, Effect of the damping function in dispersion corrected density functional theory, J. Comput. Chem. **32**, 1456 (2011).
[22] A. D. Becke and E. R. Johnson, A simple effective potential for exchange, J. Chem. Phys. **124**, 221101 (2006).
[23] H. B. Schlegel, Optimization of equilibrium geometries and transition structures, J. Comput. Chem. **3**, 214 (1982).
[24] H. J. Monkhorst and J. D. Pack, Special points for Brillouin-zone integrations, Phys. Rev. B **13**, 5188 (1976).
[25] X. Gonze and C. Lee, Dynamical matrices, Born effective charges, dielectric permittivity tensors, and interatomic force constants from density-functional perturbation theory, Phys. Rev. B **55**, 10355 (1997).
[26] S. J. Clark, M. D. Segall, C. J. Pickard, P. J. Hasnip, M. I. Probert, K. Refson, and M. C. Payne, First principles methods using CASTEP, Z. Kristallogr. **220**, 567 (2005).
[27] G. J. Martyna, M. L. Klein, and M. Tuckerman, Nosé–Hoover chains: The canonical ensemble via continuous dynamics, J. Chem. Phys. **97**, 2635 (1992).
[28] H. C. Andersen, Molecular dynamics simulations at constant pressure and/or temperature, J. Chem. Phys. **72**, 2384 (1980).
[29] W. G. Hoover, Canonical dynamics: Equilibrium phase-space distributions, Phys. Rev. A **31**, 1695 (1985).
[30] W. G. Hoover, Constant-pressure equations of motion, Phys. Rev. A **34**, 2499 (1986).
[31] G. J. Martyna, D. J. Tobias, and M. L. Klein, Constant pressure molecular dynamics algorithms, J. Chem. Phys. **101**, 4177 (1994).
[32] S. Grimme, Semiempirical GGA-type density functional constructed with a long-range dispersion correction, J. Comput. Chem. **27**, 1787 (2006).
[33] X. Gonze, G.-M. Rignanese, M. Verstraete, J.-M. Beuken, Y. Pouillon, R. Caracas, F. Jollet, M. Torrent, G. Zerah, M. Mikami *et al.*, A brief introduction to the ABINIT software package, Z. Kristallogr. **220**, 558 (2005).
[34] G. Onida, L. Reining, and A. Rubio, Electronic excitations: Density-functional versus many-body Green's-function approaches, Rev. Mod. Phys. **74**, 601 (2002).
[35] R. W. Godby and R. J. Needs, Metal-Insulator-Transition in Kohn-Sham Theory and Quasiparticle Theory, Phys. Rev. Lett. **62**, 1169 (1989).
[36] M. Fuchs and M. Scheffler, *Ab initio* pseudopotentials for electronic structure calculations of poly-atomic systems using density-functional theory, Comput. Phys. Commun. **119**, 67 (1999).
[37] H. Schulz and K. H. Thiemann, Crystal-structure refinement of AlN and GaN, Solid State Commun. **23**, 815 (1977).
[38] C. Stampfl and C. G. Van de Walle, Density-functional calculations for III-V nitrides using the local-density approximation and the generalized gradient approximation, Phys. Rev. B **59**, 5521 (1999).
[39] A. F. Wright and J. S. Nelson, Explicit treatment of the gallium 3*d* electron in GaN using the plane-wave pseudopotential method, Phys. Rev. B **50**, 2159 (1994).
[40] F. Ortmann, F. Bechstedt, and W. G. Schmidt, Semiempirical van der Waals correction to the density functional description of solids and molecular structures, Phys. Rev. B **73**, 205101 (2006).
[41] T. Hanada, in *Oxide and Nitride Semiconductors*, edited by T. Yao and S.-K. Hong (Springer, Berlin, 2009), p. 5.
[42] C. Bungaro, K. Rapcewicz, and J. Bernholc, *Ab initio* phonon dispersions of wurtzite AlN, GaN, and InN, Phys. Rev. B **61**, 6720 (2000).
[43] T. Ruf, J. Serrano, M. Cardona, P. Pavone, M. Pabst, M. Krisch, M. D'Astuto, T. Suski, I. Grzegory, and M. Leszczynski, Phonon Dispersion Curves in Wurtzite-Structure GaN Determined by Inelastic X-ray Scattering, Phys. Rev. Lett. **86**, 906 (2001).
[44] J. M. Zhang, T. Ruf, M. Cardona, O. Ambacher, M. Stutzmann, J. M. Wagner, and F. Bechstedt, Raman spectra of isotopic GaN, Phys. Rev. B **56**, 14399 (1997).
[45] A. Rubio, J. L. Corkill, M. L. Cohen, E. L. Shirley, and S. G. Louie, Quasi-particle band-structure of AlN and GaN, Phys. Rev. B **48**, 11810 (1993).
[46] D. Vogel, P. Kruger, and J. Pollmann, Structural and electronic properties of group-III nitrides, Phys. Rev. B **55**, 12836 (1997).
[47] B. J. Min, C. T. Chan, and K. M. Ho, 1st-principles total-energy calculation of gallium nitride, Phys. Rev. B **45**, 1159 (1992).
[48] S. S. Dhesi, C. B. Stagarescu, K. E. Smith, D. Doppalapudi, R. Singh, and T. D. Moustakas, Surface and bulk electronic structure of thin-film wurtzite GaN, Phys. Rev. B **56**, 10271 (1997).
[49] T. P. Chow and M. Ghezzo, in *III-Nitride, SiC, and Diamond Materials for Electronic Devices*, Vol. 423 of *Materials Research Society Symposium Proceedings*, edited by D. K. Gaskill, C. D. Brandt, and R. J. Nemanich (Materials Research Society, Pittsburgh, 1996), p. 10.
[50] B. J. Morgan, Preferential stability of the d-BCT phase in ZnO thin films, Phys. Rev. B **80**, 174105 (2009).